

PROFILE EVOLUTION OF EDGE PARAMETERS DURING L/H AND H/L MODE TRANSITIONS ON COMPASS-D*)

H. MEYER, P.G. CAROLAN, N. J. CONWAY, A. R. FIELD, S.J. FIELDING,
P. HELANDER

*EURATOM/UKAEA Fusion Association, Culham Science Centre, Abingdon,
Oxfordshire, OX14 3DB, UK*

Received 9 June 2000
final version 18 September 2000

On COMPASS-D the profile evolution of electron density, electron temperature, perpendicular electric field, poloidal impurity velocity, and neutral density at the outboard mid-plane has been investigated during ohmic single null diverted (SND) discharges undergoing an L/H, H/L, and another L/H transition. This was achieved using a novel combined diagnostic consisting of thermal helium beam and Doppler spectrometry, sharing the same lines of sight. To generate the transitions first an ELM-free H-mode phase was produced by terminating the gas fuelling. Within this H-mode a stepped gas puff was applied triggering an intermediate L-mode phase followed by a second ELM-free phase. It was found that on COMPASS-D the L/H transition is not preceded by a change in velocity or electric field shear. The maximum electric field shear of $\nabla E_\psi \approx 2 \times 10^3 \text{ kV/m}^2$ develops after the L/H transition around the 95% flux surface. Although the neutral density at the separatrix is of the order $n_D \approx 10^{17} \text{ m}^{-3}$ no indication of a local influence could be concluded. However, a correlation between the decay of the shear and the gas puff was observed.

1 Introduction

In many magnetically confined fusion experiments a transition from a *low-confinement* L-mode to a *high-confinement* H-mode is observed [1, 2]. The H-mode is a favoured operating regime for a future fusion power plant but the occurrence of edge localized modes (ELMs) producing high heat fluxes and the loss of density control points to a need to understand and hopefully control the transition between L- and H-mode. Although the ubiquity of the H-mode suggests rather robust common edge conditions this understanding is still lacking. In recent years many H-mode transition theories have been developed but none of them is completely satisfactory [3]. In particular the influence of neutral particles and the causality of events are controversial subjects. It is widely believed that a sheared perpendicular electric field and the associated sheared poloidal (and toroidal) plasma flows observed in the H-mode phase account for the reduction of turbulent cross field transport. To check the theories and deepen the understanding of the physics underlying the transition detailed experimental data is necessary.

*) Presented at the Workshop on Role of Electric Fields in Plasma Confinement and Exhaust, Budapest, 18–19 June 2000.

The difficulties in obtaining such detailed data are due to the fast time scales associated with ELMs, the abrupt transition into ELM-free phases, and the dependence on the gradients of important edge parameters such as electron density, n_e , electron temperature, T_e , ion temperature, T_i , poloidal velocity, $v_{i\theta}$, toroidal velocity, $v_{i\phi}$, the “radial” electric field, E_ψ , and neutral (atomic) density n_D . Hence a fast time resolution, of a few milliseconds, and a high spatially resolution, of a few millimeters, is required. Such resolution has now been achieved on COMPASS-D using a combined diagnostic [4] consisting of a thermal helium beam diagnostic (HELIOS) [5] and a high resolution spectrometer (CELESTE) [6]. Both fast spectroscopic diagnostics observe the same spatial region at the plasma boundary by sharing the same optics. Among other things profiles of n_e , T_e , n_D , E_ψ , and $v_{z\theta}$ where z denotes the observed impurity species can be obtained from this diagnostic.

In what follows we present first results of the evolution of the above profiles for a series of ohmic SND discharges during a sequence of L-mode, ELM-free H-mode, L-mode, and a second ELM-free H-mode. This was achieved by applying a stepped gas puff within an ELM-free H-mode generated by terminating the gas fuelling. The additional gas puff triggers an H/L transition which is followed by a subsequent L/H transition after the gas puff. This gives the opportunity to observe three transitions in a single discharge.

2 Diagnostic and analysis

The novel combined HELIOS/CELESTE diagnostic [4] on COMPASS-D consists of a thermal helium beam spectrometry (HELIOS) [5] sharing the same optics with a Doppler spectrometry (CELESTE) [6], observing the plasma boundary at the outboard mid-plane (see Fig. 1). From the HeI line ratios delivered by HELIOS n_e and T_e can be calculated at 10 equidistant radial positions ($\Delta r = 6$ mm) using atomic data from ADAS [7]. For the collisional radiative modelling a Maxwellian

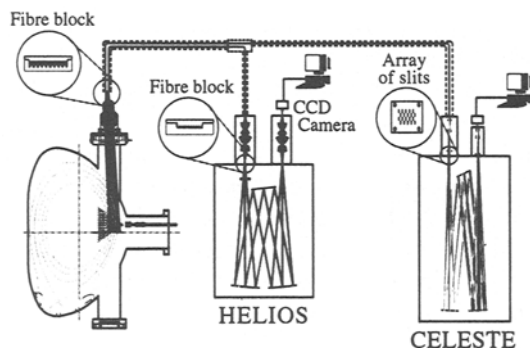


Fig. 1. Schematic of the HELIOS/CELESTE diagnostic. Note that the lines of sight are not crossing the divertor region avoiding regions with strong localized neutral sources.

distribution is assumed. The effect of e.g. 10% super-thermal electrons at $T_e^s = 10 T_e$ is less than 10% for temperatures above 20 eV [8]. The time resolution used here was $\Delta t = 5$ ms but can be reduced to $\Delta t = 2$ ms. In addition, the absolute D_α -intensity is recorded from which n_D can be deduced (see Sec. 2.1). The multi-chord, high-resolution CELESTE spectrometer provides the spectral line profile of an impurity species on 19 lines of sight ($2 \text{ mm} \leq \Delta r \leq 5 \text{ mm}$) in the same plasma region as HELIOS. This provides information on the relative intensity \tilde{I}_z , $v_{z\theta}$, and T_z from the height, shift, and width of the line respectively. Here, the emission of HeII at the resonance line at $\lambda_0 = 468.67 \text{ nm}$ was recorded with a time resolution of $\Delta t = 2.5 \text{ ms}$ (maximum $\Delta t \approx 1 \text{ ms}$). HeII is locally produced by the thermal helium beam ($\lambda_{\text{ion}}(0 \rightarrow 1^+) \approx 3 \text{ mm}$). These ions are further ionized after $\lambda_{\text{ion}}(1^+ \rightarrow 2^+) \approx 3 \text{ m}$ which is smaller than the toroidal diameter $2\pi R \approx 4.6 \text{ m}$ on COMPASS-D. Hence, the HeII emission detected is essentially localized to the beam.

2.1 Deducing the neutral density

The D_α -intensity is line integrated and the data needs to be inverted to obtain a radial emission profile, ϵ . The 10 chords from HELIOS are not adequate for tomographic reconstruction. However, by assuming that the emission is a flux quantity $\epsilon = \epsilon(\psi)$, i.e. constant on surfaces of constant poloidal magnetic flux Ψ_p , we can invert the intensity. Here, $\psi = \Psi_p/2\pi$ is the poloidal flux function (see also Subsect. 2.2). Although the D_α -emission is generally not a flux quantity the above assumption is a reasonable approximation over the limited observed region. This is because on the one hand at the outboard mid-plane T_e and n_e are good flux quantities even outside the confined region and on the other hand over the small observed region the neutral influx from the wall is approximately constant.

For sampled data the inversion can be formulated as matrix equation

$$\mathbf{i} = \mathbf{L} \cdot \boldsymbol{\epsilon}, \quad (1)$$

where \mathbf{i} is the intensity vector, $\boldsymbol{\epsilon}$ the emissivity vector, and \mathbf{L} is the length matrix. The latter can be calculated numerically for each time point using ψ from an EFIT equilibrium construction [9]. Therefore, the flux function is divided in j shells determined by the radial positions for which ϵ_j is required. The matrix element L_{ij} is then given by the length of the i -th line of sight in the j -th flux shell. Instead of inverting Eq. (1) directly it is better to use a maximum entropy fit algorithm [10]. After calculating the emission the neutral density was derived by applying the collisional-radiative model [11].

2.2 Flux coordinates

Many quantities including n_e , T_e , and E in the confined region of a tokamak are constant on poloidal flux surfaces. As can be seen from Figure 2 showing the evolution of the profile of the normalized flux function $\psi_N = (\psi - \psi_0)/(\psi_S - \psi_0)$

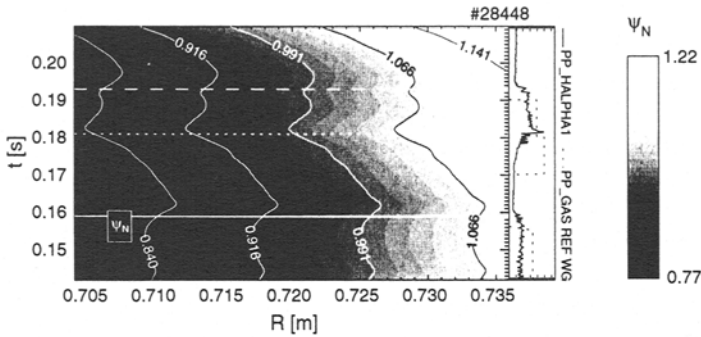


Fig. 2. Evolution of the radial profile of the normalized flux ψ_N in the observed region for shot 28448. The horizontal lines mark the transition times as can be seen from the D_α trace (right).

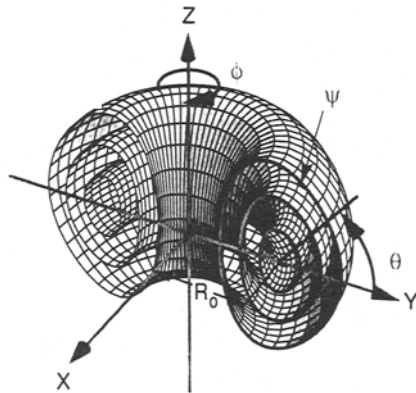


Fig. 3. Definition of flux coordinates.

(ψ_0 — value of ψ at the magnetic axis; ψ_S — value of ψ at the separatrix) within the observed region for shot 28448 the flux surface positions change in time. To mark the different phases of the shot traces of the D_α -intensity at the mid-plane and the reference waveform of gas puff are shown at the right edge.

It is therefore useful to introduce flux coordinates (ψ, θ, ϕ) as shown in Fig. 3 with $\psi(R, Z; t)$ — the poloidal flux function, and $\theta(R, Z; t) = \tan^{-1}[(Z - Z_0)/(R - R_0)]$ — the usual poloidal angle; $R_0(t)$ and $Z_0(t)$ correspond to the position of the magnetic axis and $\phi = -\varphi$ is the toroidal angle defined opposite to the one for the usual cylindrical machine coordinate system (R, φ, Z) — see Ref. 12 for details.

The flux coordinate system is uniquely defined by the unit vectors

$$\mathbf{e}^\psi = \frac{\nabla\psi}{|\nabla\psi|}, \quad \mathbf{e}^\theta = \frac{\nabla\theta}{|\nabla\theta|}, \quad \mathbf{e}^\phi = -\mathbf{e}^\varphi, \quad (2)$$

following the notation in [12]. Note, that \mathbf{e}^ψ and \mathbf{e}^θ are not orthogonal to each other. We used an EFIT equilibrium reconstruction [9] for calculating the unit vectors for each time step. At the mid-plane this coordinate system, though strictly only defined on closed flux surfaces, can be extended into the scrape of layer (SOL).

2.3 The electric field

The impurity velocity measured by CELESTE in general differs from the velocity of the ions. A more fundamental quantity is the electric field which all ion species experience. We derive the electric field from the momentum balance equation for the impurity species $z = \text{HeII}$

$$\mathbf{E} = \underbrace{-\mathbf{v}_z \times \mathbf{B}}_{\text{Lorentz}} + \underbrace{\frac{\nabla p_z}{Z_z e n_z}}_{\text{dia.}} + \underbrace{\frac{m_z(\mathbf{v}_z \cdot \nabla)\mathbf{v}_z}{Z_z e}}_{\text{inertia}} + \underbrace{\frac{\nabla \cdot \boldsymbol{\pi}}{Z_z e n_z}}_{\text{visc.}} + \underbrace{\frac{\mathbf{R}_{z0}}{Z_z e n_z}}_{\text{neutral fric.}} + \underbrace{\frac{\sum_\beta \mathbf{R}_{z\beta}}{Z_z e n_z}}_{\text{coulomb fric.}}. \quad (3)$$

Only the contribution from the Lorentz force $-\mathbf{v}_z \times \mathbf{B}$ and the pressure gradient $\nabla p_z/(Z_z e n_z)$ have to be considered since the other terms, normalized to the pressure gradient term, scale as follows: inertia $\propto M_z^2 \approx 0.04$, perpendicular viscosity $\propto M_z \rho_z / L_\perp \approx 0.07$, neutral friction $\propto M_z L_\perp / \lambda_{zn} \approx 3 \times 10^{-6}$, coulomb friction $\propto M_z L_\perp / \lambda_{zi} \approx 5 \times 10^{-5}$ where $M_z = v_{z\theta} / v_{zth}$, ρ_z the Larmor radius, L_\perp the typical pressure gradient length, and $\lambda_{\alpha\beta}$ the mean free path for collisions between particles of species α and species β . Also the contribution arising from the toroidal velocity v_ϕ can be neglected. This is because on COMPASS-D the toroidal velocity is usually smaller than v_θ [13] and being weighted with $B_\theta/B_\phi \approx 0.1$ it is negligible. Therefore, the radial electric field can be reasonably approximated by

$$E_\psi = \frac{\nabla p_z \cdot \mathbf{e}^\psi}{Z_z e n_z} - v_{z\theta} B_\phi. \quad (4)$$

To calculate the diamagnetic term $(\nabla p)/n = T[L_n^{-1} + L_T^{-1}]$, where L_n , L_T are the density and temperature gradient lengths respectively, $L_n = (\nabla \ln n)^{-1}$ has to be deduced from the measured intensity profile. Therefore we invert the intensity to obtain an emission profile and apply a full collisional radiative model to calculate the relative impurity density profile.

3 Results

3.1 Shot preparation

Figure 4 shows time traces for the shots 28443 (gray; without gas puff), and 28447 (black; with gas puff) of (a) plasma current I_P , (b) line averaged density \bar{n}_e , (c)

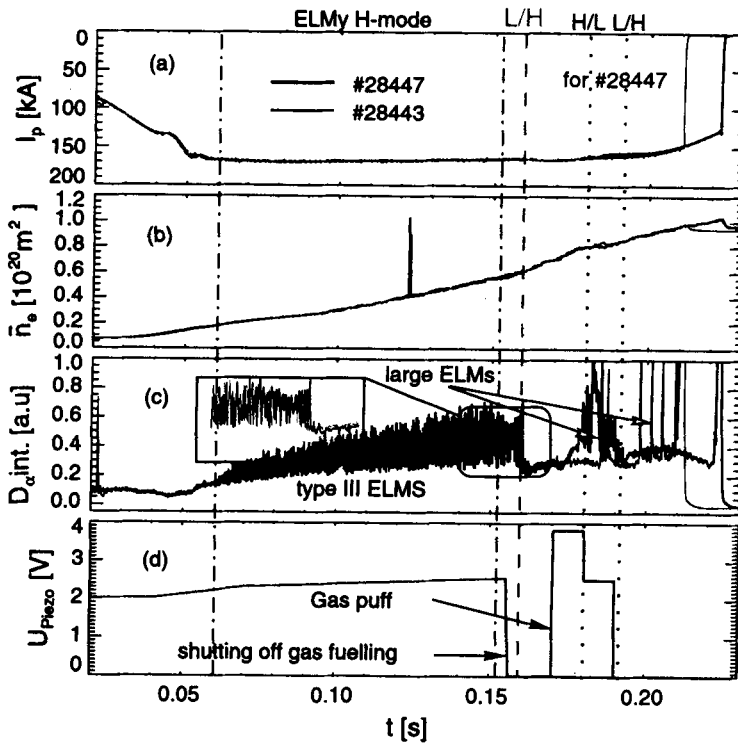


Fig. 4. Time traces (a) plasma current, (b) line-averaged density, (c) D_{α} -intensity, and (d) reference waveform for the gas fuelling for the COMPASS-D shots no. 28447 (with gas puff) and 28443 (without gas puff).

averaged D_{α} -intensity through X-Point, and (d) the driving voltage of the piezo valve U_{Piezo} controlling the inlet of deuterium. The sudden drop of the D_{α} -emission at $t \approx 0.16$ s (trace b) indicates the transition from L-mode into an ELM-free H-mode 3 ms after termination of the gas fuelling.

In ohmic discharges on COMPASS-D usually a gradual transition between L-mode and ELM-free H-mode through a “dithering” ELMy phase is observed and here the D_{α} traces (c) show type III ELMS before the ELM-free phase. However, as indicated by the detail in Fig. 4, the plasma is close or even in full L-mode just before the transition due to the sustained fuelling and the increasing density.

In shot 28447 a stepped gas puff was applied at $t_3 = 0.18$ s (trace d). The bigger first-part ($\Delta t = 10$ ms) triggers a H/L-transition which then is sustained by the slightly smaller back-part ($\Delta t = 10$ ms). After the gas is shut-off the plasma enters again into an ELM-free H-mode. Of interest is that the large ELMS which occur in the shot without the gas puff are absent when a gas puff is applied (see Fig. 4, trace c).

3.2 Poloidal impurity velocity

Figures 5 and 6 show time traces of the poloidal velocity along surfaces of constant normalized flux. To illustrate the different phases of the shot the D_α -intensity and U_{Piezo} are also shown. Note that the time points are chosen to be at the end of the integration period to avoid confusion with the causality of events. The two discharges were similar except that the second-part of the gas puff in shot 28448 was higher, leading to a prolonged intermediate L-mode phase. The most striking feature is that there is no evidence for a change in velocity shear prior to the L-H

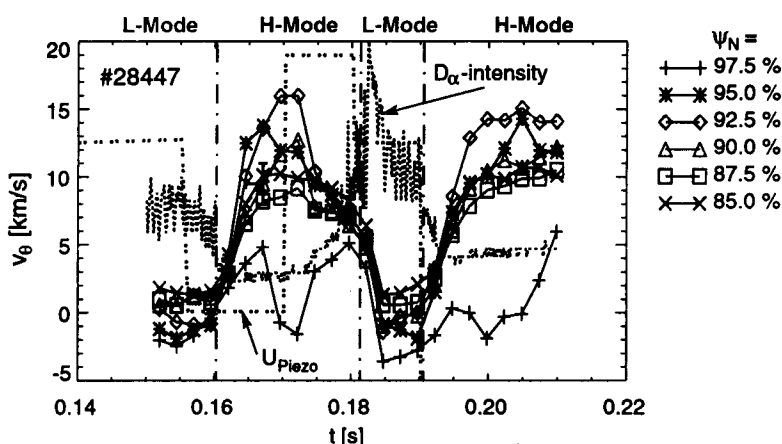


Fig. 5. Time traces of the poloidal velocity along constant flux surfaces for shot 28447. Also the D_α -intensity and U_{Piezo} are shown.

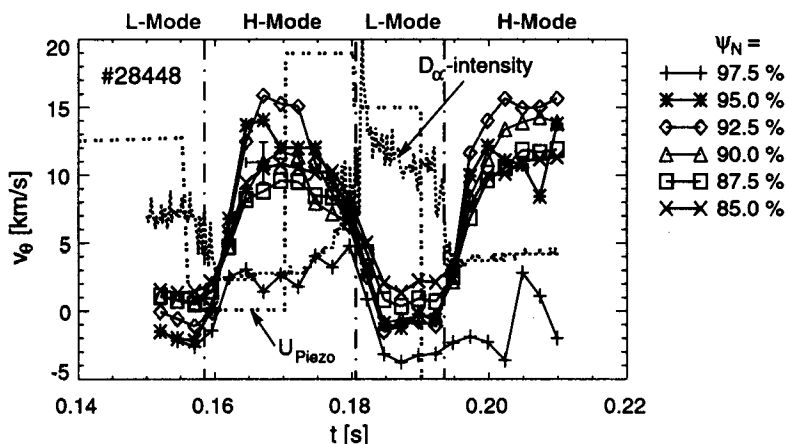


Fig. 6. Same as in Fig. 5 for shot 28448.

transitions within the observed region. A significant shear only develops *after* the plasma has entered the H-mode. This can also be seen from Fig. 8 showing E_ψ . Nevertheless, the importance of the velocity on the H/L-transition shear is evident. Here, the velocity shear starts to decrease coincident with the onset of the gas puff. Only when the shear has fallen to a small value does the plasma undergo the transition.

Figure 7 shows the evolution of the profile of the poloidal impurity velocity for shot 28448 in a contour plot with the flux radius, $\sqrt{\psi_N} \sim r/a$ as abscissa (compare to Fig. 6). There is a clear maximum at the 92% flux surface leading to two regions of velocity shear: a negative shear region located at the 95% flux surface and a positive shear region located at the 90% flux surface. But these extrema in the impurity velocity are not reflected in the electric field (see Fig. 8).

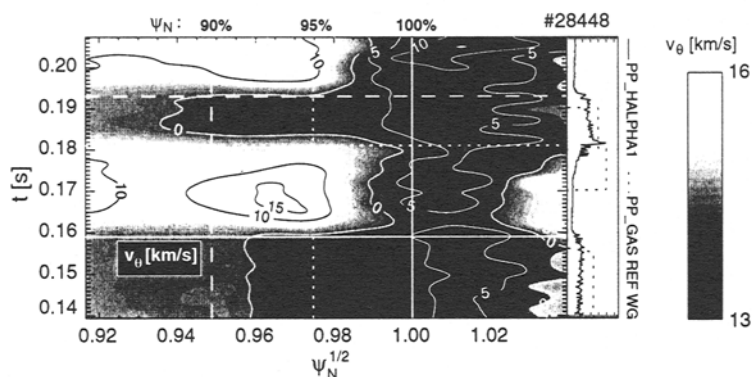


Fig. 7. Evolution of the profile $v_{z\theta}$ for shot 28448 as contour plot with $\sqrt{\psi_N} \sim r/a$ as abscissa. The vertical lines mark the 90%, 95%, and 100% flux surface and the horizontal lines the transition times.

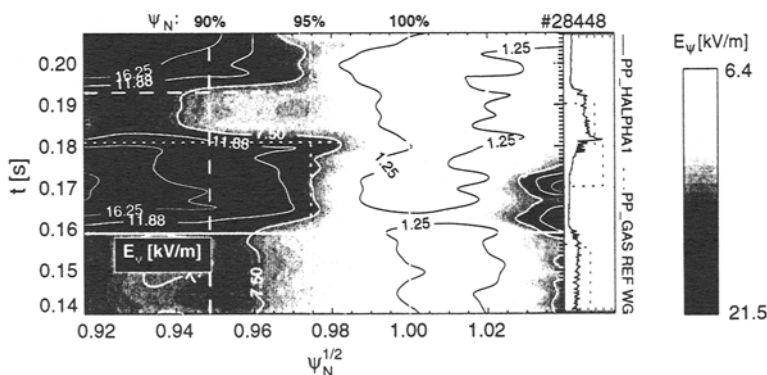


Fig. 8. Evolution of the profile of E_ψ presented similar to Fig. 7.

The HeII velocity can however differ markedly from the plasma ion velocity. Using Eq. (4) we can calculate the radial electric field which all ion species experience. The evolution of the E_ψ -profile is shown in Fig. 8. Within the confined region E_ψ points inwards with higher values in the H-mode phase and a maximum change of $\Delta E_\psi \approx -12$ kV/m. Although the velocity clearly has a maximum around the 92% flux surface (see Fig. 7) no minimum of E_ψ occurs.

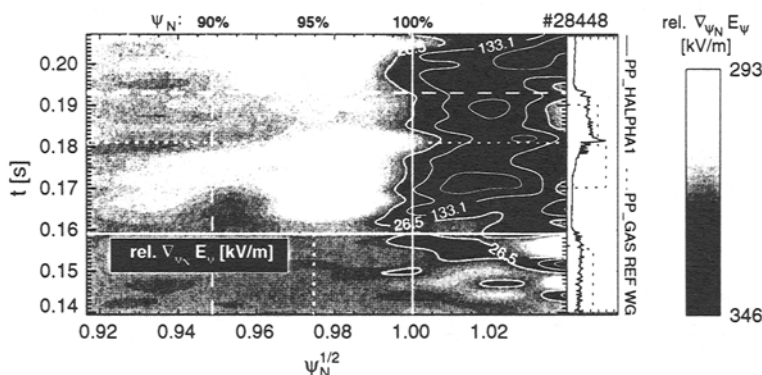


Fig. 9. Evolution of the profile of the shear of the electric field relative to the average shear between $t = 140$ ms and $t = 155$ ms for shot 28448 presented similar to Fig. 7.

The maximum shear in the electric field of $\partial E_\psi / \partial r \approx 2 \times 10^3$ kV/m² is around the 96% flux surface as can be seen from Fig. 9 showing the change of $\partial E / \partial \psi_N$ with respect to the first L-mode phase from $t = 140$ s to $t = 155$ ms. Note, that even in the L-mode phase the electric field already exhibits shear in this region although the shear in $v_{z\theta}$ is negligible. But, after the L/H-transition this shear increases. Correlated with the onset of the gas puff the shear starts to decay clearly before the H/L-transition. From the behaviour of the local neutral density shown in Fig. 11 we regard it as unlikely that this decay of shear corresponds directly to changes in the local neutral density. However, the accuracy of the neutral density data this far inside the plasma is not sufficient to produce clear evidence.

Figures 10 and 11 show the evolution of n_e and n_D , respectively. As expected, the electron density inside the separatrix is higher in the H-mode than in L-mode. But, interestingly, the opposite is true outside the separatrix in the SOL. This is more pronounced in the triggered L-mode between $t = 0.18$ s to $t = 0.19$ s. The neutral density (Fig. 11) shows an opposite behaviour, with the neutral density profile extending further into the plasma in L-mode than in H-mode. However, the changes of the neutral density rather seem to succeed the transition whereas the n_e -evolution is more correlated to the evolution of E_ψ . The observation that the n_D profile develops after the L/H and H/L transitions does not support a local influence of n_D on shear. The fact that both electron and neutral density decrease at the separatrix suggest that the mean energy of the influx neutrals has decreased in H-mode compared to L-mode.

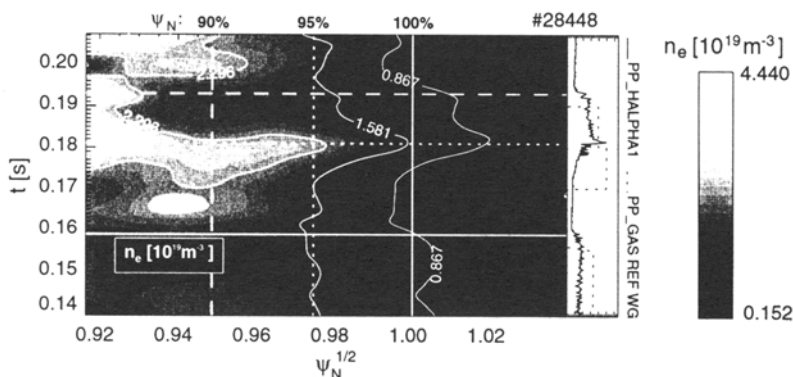


Fig. 10. Evolution of the profile of n_e for shot 28448 presented similar to Fig. 7.

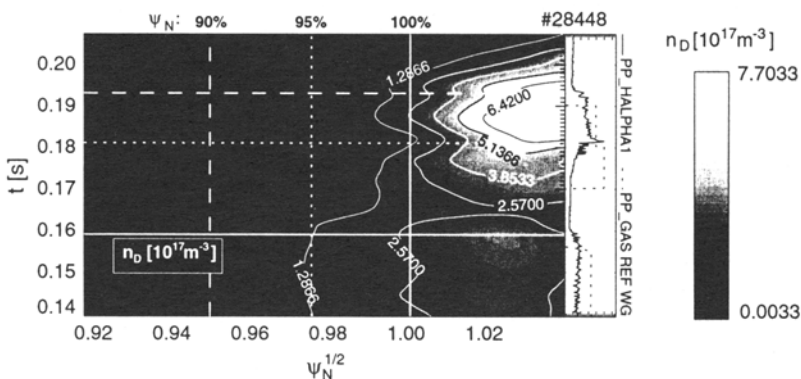


Fig. 11. Evolution of the profile of n_D for shot 28448 presented similar to Fig. 7.

4 Conclusions

We presented first result from a detailed analysis of the profile evolution of the impurity velocity, the perpendicular electric field, the electron density and the neutral density. At this stage of the analysis no significant change of these analysed parameters prior to the H-mode was found. All the quantities show the same behaviour at both observed L/H transitions. At least on COMPASS-D the high velocity and electric field shear clearly evolve around the 95% flux surface *only after* the L/H-transition on a time scale of ≈ 10 ms. On the other hand the H/L-transition is preceded by a decay of the shear in this region correlated to the onset of the gas puff. Whether this decay is caused by a change in the local neutral density or not can not be deduced from our data. However, we regard this as unlikely since our data indicates that the evolution of n_D at the mid-plane is *subsequent* to the L/H and H/L-transition. The neutral density at the separatrix was found to be quite

high with $n_D \approx 2.5 \times 10^{17} \text{ m}^{-3}$ in L-mode and $n_D \approx 1.7 \times 10^{17} \text{ m}^{-3}$ in H-mode. The gradient lengths of both n_D and n_e are shorter in H-mode than in L-mode and both quantities are reduced at the separatrix in H-mode suggesting that the mean energy of the influx neutrals is reduced in H-mode.

This work was jointly funded by the UK Department of Trade and Industry and EURATOM. The author H. Meyer is funded by a Marie Curie Research Training Grant.

References

- [1] F. Wagner et al.: Phys. Rev. Lett. **49** (1982).
- [2] ASDEX-Team: Nucl. Fusion **29** (1989) 1959.
- [3] J.W. Connor and H. R. Wilson: Plasma Phys. Control. Fusion **42** (2000).
- [4] P.G. Carolan, N. J. Conway, A. R. Field, and H. Meyer: submitted for publication in Rev. Sci. Instrum.
- [5] A.R. Field, P.G. Carolan, C.N. J., and O.M. G: Rev. Sci. Instrum. **70** (1999) 355.
- [6] P.G. Carolan et al.: Rev. Sci. Instrum. **68** (1997) 1015.
- [7] H.P. Summers and M. von Hellermann: in *Atomic and plasma-material interaction processes in controlled thermonuclear fusion*. (Eds. R.K. Janev and H.W. Drawin). Elsevier Science Publishers B. V., Amsterdam, 1993.
- [8] M. Brix: Technical Report No. JUL 3638, Institut für Plasmaphysik, Forschungszentrum Jülich (unpublished).
- [9] L.L. Lao et al.: Nuclear Fusion **25** (1985) 1611.
- [10] J. Skilling and S. Gull: Technical Report No. CUL 3130, Cambridge University, Dept. Applied Mathematics and Theoretical Physics (unpublished).
- [11] K. Sawada, K. Eriguchi, and T. Fujimoto: J. Appl. Phys. **73** (1993) 8122.
- [12] R.D. Hazeltine and M.J. D.: *Plasma Confinement* (Frontiers of Physics, Vol. 86). Addison-Wesley Publishers, New York, 1992.
- [13] P. G. Carolan et al.: in *22nd European Physical Society Conference on Controlled Fusion and Plasma Physics*. European Physical Society, Europhysics Letters **21a** (1995) 273.